

SUPPLEMENTARY INFORMATION

DOI: 10.1038/NPHYS435

1

In the format provided by the authors and unedited.

Reply to the Comment by Shprits et al. on the manuscript "Explaining the dynamics of the ultra-relativistic third Van Allen radiation belt" by Mann et al., Nature Physics, (2016)

Supplementary Information

I.R. Mann¹, L.G. Ozeke¹, S. K. Morley², K. R. Murphy^{1,3}, S. G. Claudepierre⁴, D. L. Turner⁴, D. N. Baker⁵, I.J. Rae⁶, A. Kale¹, D.K. Milling¹, A.J. Boyd^{7,8}, H. E. Spence⁷, H. J. Singer⁹, S. Dimitrakoudis^{1,10}, I. A. Daglis^{11,10} and F. Honary¹²

It is well-known that there are many wave-particle interaction processes which have the potential to affect the dynamics of the radiation belts [see e.g., the review by Mauk et al., 2013]. The issue that has continued to obstruct significant advances in our understanding of the

¹Department of Physics, University of Alberta, Edmonton, AB, T6G 2G7. Canada.

²Space Science and Applications (ISR 1), Los Alamos National Laboratory, Los Alamos, NM 87545, USA.

³NASA Goddard Spaceflight Center, Code 674, Greenbelt, Maryland, MD 20771, USA.

⁴The Aerospace Corporation, Los Angeles, CA 90009, USA

⁵Laboratory for Atmospheric and Space Physics, University of Colorado, Boulder, CO 80309, USA

⁶Mullard Space Science Laboratory, University College London, Holmbury St. Mary, Dorking, Surrey, RH5 6NT, UK.

⁷Institute for the Study of Earth, Oceans, and Space, University of New Hampshire, Durham, NH 03824-3525, USA

⁸The New Mexico Consortium, Los Alamos, NM 87544, USA.

⁹Space Weather Prediction Center, NOAA, Boulder, Colorado, 80305, USA.

¹⁰National Observatory of Athens, Institute for Astronomy, Astrophysics, Space Applications and Remote Sensing, 15236, Penteli, Greece.

¹¹Department of Physics, National and Kapodistrian University of Athens, 15784 Athens, Greece.

¹²Department of Physics, Lancaster University, Lancaster, U.K.

radiation belts to the point of predictability is our ability to represent the nature of the magnetospheric processes controlling belt dynamics with sufficient accuracy to establish which dominate. In relation to the case examined here it is to determine which process or processes can act to create a third Van Allen radiation belt morphology in September 2012 as reported by Baker et al., (2013). As described in the main text of our Reply, and further expanded upon in the Supplementary Material presented here, we show that the original conclusion from Mann et al. (2016) remains valid. That is, a remnant belt and the third radiation belt morphology which arises following a subsequent flux recovery at higher L-shells, can be explained by the action of very fast outwards ULF wave radial diffusion associated with magnetopause shadowing. Contrary to the claims of the Comment by Shprits et al. (2017; hereafter S17), and the conclusions of modelling by Shprits et al. (2013; hereafter S13), the action of EMIC waves is not required.

The presence of EMIC Waves?

In order to associate the losses with EMIC waves as proposed by S17, then such waves might be expected to be observed at the appropriate location at the right time. Neither the S17 Comment nor S13 provide any observational evidence for the presence of the required EMIC waves with the appropriate amplitude in the right place. The modelling in S13 introduced, without observational support, EMIC wave penetration as low as L=3 to provide the localised losses around L*~3-4 need to create the remnant belt. EMIC wave amplitudes were taken from observations at much higher geosynchronous altitudes, and were applied for a continuous period from 00UT on September 03, 2012 until 03UT on September 05, 2012. In contrast, in our

original Mann et al. (2016) paper we used observations to constrain the ULF wave power and which in our model created a remnant belt through enhanced ULF wave outward radial diffusion.

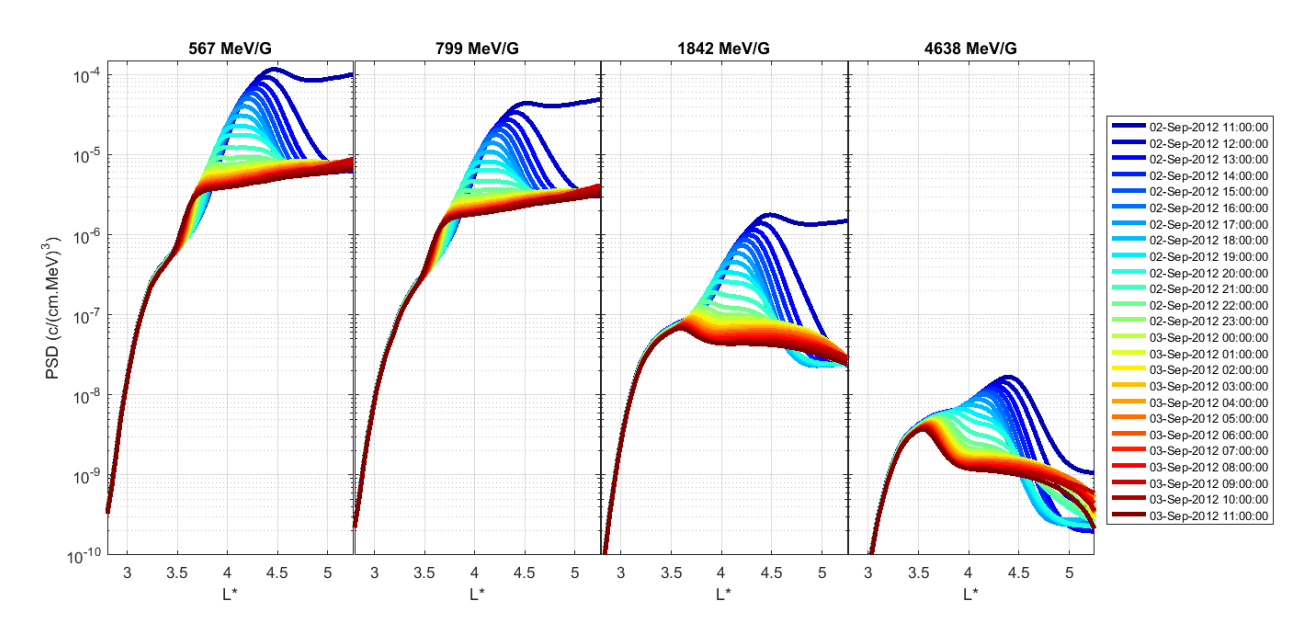
The Importance of the Accurate Specification of ULF Wave Power

The authors of S17 draw reference to the earlier modelling work presented in S13 which adopts the empirical statistical Brautigam and Albert (2000) representation for the rates of radial diffusion in their model. As shown in our original Mann *et al.* (2016) article, statistical approaches may not be able to accurately characterise the ULF wave power in the magnetosphere at storm times (see also e.g., Dimitrakoudis et al., 2015; Murphy *et al.*, 2016). As shown in the comparison between the observed ULF wave fields and those from empirical statistical representation shown in Supplementary Material Figure 1 in Mann *et al.* (2016), the S13 modelling will significantly under-estimate the impacts of ULF wave transport during this storm especially during the period of strong loss in the main phase. More generally and perhaps even more importantly, and as we have recently discussed elsewhere (e.g., Mann and Ozeke, 2016), radiation belt models which do not include accurate representations of some of the important physical processes cannot be reliably used to discriminate those with dominant impacts from those which only have a rather incremental effect.

Despite these facts, S17 use the results from S13 to criticise the simulation results in Mann *et al.* (2016), claiming that enhanced ULF wave outward transport cannot produce a belt as narrow as observed. However, as discussed for example by O'Brien *et al.* (2015), ultra-relativistic energy spectra are very steep such that there can be large flux changes even inside a single energy bin. Mapping from phase space density (PSD) in model domains into flux for comparison with observations can hence be a sensitive function of energy. Moreover, as

discussed in detail in Mann *et al.* (2016), we also used a relatively simple axisymmetric dipolar field model to map the ground-based ULF wave power used to specify the rates of diffusion of electrons in the equatorial plane. Together these affects might impact the accuracy of our simulation results, including as a function of energy.

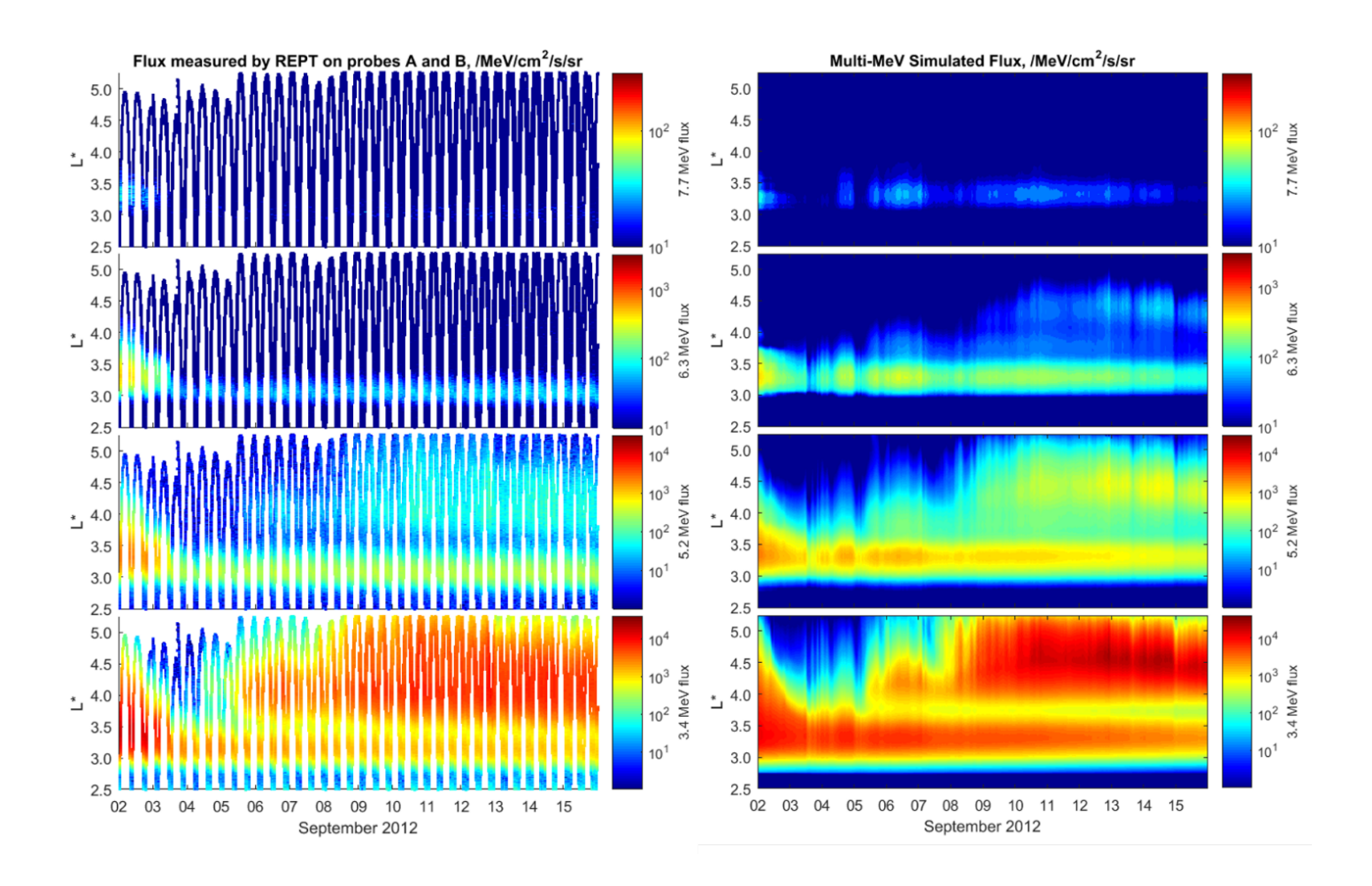
Nonetheless, Supplementary Figure 1 which shows additional magnetopause shadowing simulation runs using the same approach described in Ref. 1, demonstrates clearly how such outward radial ULF wave transport can cause erosion of the outer belt. Moreover, as also shown in Supplementary Figure 1, radial diffusion can naturally create both monotonic and non-monotonic PSD profiles without invoking EMIC wave effects – but which Shprits *et al.*² assert must be due to the energy dependence of EMIC wave loss. Indeed, once the PSD recovers at the outer boundary this will produce a dipped PSD profile like that observed.



Supplementary Fig. 1. Simulated PSD profiles as a function of L*. Results for four different first adiabatic invariants from radial diffusion simulations demonstrating the impacts of datadriven flux decreases at the outer boundary. The model results show the creation of the remnant belt in the inner magnetosphere at higher first invariant, and monotonic PSD profiles at lower first invariant due to energy dependent boundary conditions and without requiring the action of EMIC wave loss. Later recovery of the PSD at high L* for the higher first invariants regenerates the higher L* outer belt, creating the third belt morphology.

SUPPLEMENTARY INFORMATION

To contrast with other comments on our work by S17, Supplementary Figure 2 shows that our model produces a narrow isolated remnant belt, whose thickness decreases with energy, very similar to the Van Allen Probe observations at energies up to 7.7 MeV. Our results can also be compared directly to the S13 simulation results presented in their Figure 1; given this comparison, and acknowledging the relative simplicity of our model, we stand by our original characterisation that the agreement between our model results observations is excellent.



Supplementary Fig. 2. Observations and radial diffusion simulations of the third belt interval up to higher energies. (left) REPT observations of the belt dynamics from Van Allen Probes A and B in the (from top to bottom) 7.7 MeV, 6.3 MeV, 5.2 MeV and 3.4 MeV channels. (right) Results from ULF wave radial diffusion simulations in the same channels using the Mann et al. (2016) methodology. Note the simulations do not include any EMIC wave losses.

Phase Space Density (PSD) Profiles Observed by Van Allen Probes

As described in the main text of our Reply, S17 place considerable emphasis on the profiles of electron phase space density (PSD). For example, they show PSD as a function of L* at fixed first (μ) and second (K) adiabatic invariants in their Figure 1 and claim the energy dependence argues in favor of an essential role for EMIC losses in producing the remnant belt - since EMIC losses are expected to be more efficient at higher energies. As shown in Supplementary Figure 1, an energy dependent flux at the outer boundary (which is observed) can also produce both monotonic and dipped PSD profiles as a result of radial diffusion. S17 also claim that the PSD profiles during the third belt interval show evidence for a deepening PSD minimum, consistent with localised EMIC wave losses, and discount the possibility that the remnant belt can be produced by radial transport. In contrast to the assertions of S17, Figure 1 of our Reply shows a different sequence events whereby the PSD at μ = 3500 MeV/G and at fixed K = 0.05 $G^{0.5}R_E$ and 0.1 $G^{0.5}R_E$ on outbound passes of the Van Allen Probes shows clear evidence for decreasing PSD with increasing L* at the time of the loss consistent with magnetopause shadowing.

Supplementary Figure 3, which expands on Figure 1 of the main article of our Reply, shows additional data from the Van Allen Probes on outbound orbits as well as the PSD profiles as a function of L* at a first adiabatic invariant of 3500 MeV/G at two fixed values of K = 0.05 $G^{0.5}R_E$ and $0.1~G^{0.5}R_E$. Equivalent in-bound orbits at 3500 MeV/G are shown in Supplementary Figure 4. We chose to show data at 3500 MeV/G in Figure 1 of the main article of our Reply, since, given the limited energy range available from the REPT instrument, this allows the

computation of PSD profiles to higher L* without using data from the 1.9 MeV channel (see footnote¹). For completeness, and for direct comparison with Figure 1 in S17, Supplementary Figures 5 and 6 show our PSD profiles and related field and orbit data for the out- and in-bound passes at 2500 MeV/G at fixed $K = 0.05 \text{ G}^{0.5}R_E$ and $0.1 \text{ G}^{0.5}R_E$.

At 2500 MeV/G similar behaviour is observed, consistent with magnetopause shadowing and outward ULF wave transport, with around 2 and 2.5 orders of magnitude decrease in PSD being seen at L*~5 at K = 0.05 $G^{0.5}$ R_E and 0.1 $G^{0.5}$ R_E, respectively, over the same interval from the initial conditions to orbit 4. Again, these losses are associated also with a monotonically decreasing profile of PSD as a function of L*, consistent with outward radial transport. Note that none of our Figures of the profiles of PSD at fixed μ and K show the peculiar and most likely unphysical turnover and variability of the PSD profiles at the highest L* seen in the Figures in Shprits *et al.* ²

In addition to showing the derived profiles of PSD at fixed first and second adiabatic invariants at $K = 0.05 \text{ G}^{0.5} R_E$ and $0.1 \text{ G}^{0.5} R_E$ in the bottom two rows, the other panels in Supplementary Figures 3, 4, 5 and 6, show important elements of the magnetic field model and the energies of the particles which are used to construct the PSD profiles. From top to bottom, the rows in each figure show as a function of L*: (top) the time of each orbital pass, (second and third rows) the energy of the particles at $K = 0.05 \text{ G}^{0.5} R_E$ and $0.1 \text{ G}^{0.5} R_E$; (fourth and fifth) the flux of 3.4 MeV energy particles at these K (in units of /MeV/cm²/s/sr); (sixth) the ratio of the TS04D model magnetic field at the spacecraft location (Bloc) to that in the model at the equator (Bmin), which provides a measure of the off-equatorial location of the measurement; (seventh)

-

¹ The ECT team is not entirely confident in the 1.9 MeV REPT energy channel, and believe that it is out of family and might not be properly calibrated. For this reason, when the ECT team creates a combined MagEIS and REPT PSD product, they do not usually include the 1.9 MeV REPT channel.

the ratio of Bloc to the magnetic field measured at the location of the probes, providing an estimate of the local accuracy of the field model used to calculate the PSD at fixed invariants; and finally (bottom two rows) the PSD at fixed $K = 0.05~G^{0.5}R_E$ and $0.1~G^{0.5}R_E$. As seen in these figures, the off-equatorial latitude of the spacecraft can have a very significant impact on the magnitude of the observed flux because of particles mirroring below the spacecraft. This also limits the lowest K which can be measured on any specific orbital pass; for example, during inbound orbit 3 the probes are too far from the equatorial plane to provide a measurement at $K = 0.05~G^{0.5}R_E$. This is the K value which S17 claim to show in their Figure 1.

An underestimate of the model magnetic field compared to observations can result in an underestimation of the PSD since the larger observed field implies that fluxes should be taken from higher energies at that μ , which would have lower flux. This appears to occur at L* >~4 on inbound orbit 4. Such effects would further reduce the PSD at high L below that shown in Supplementary Figure 4 at this time, further increasing the negative gradient consistent with losses from outward transport. Perhaps this effect might also remove the small dip in PSD seen at this time. Interestingly, Supplementary Figure 2 in S17 shows their derived PSD profiles for 3433 MeV/G and K = 0.11 $G^{0.5}R_E$; in our view the PSD profiles in their Figure also provide evidence in favour of outward transport.

Shprits *et al.*² are correct that there does appear to be a further reduction in the PSD dip between the inbound pass on orbit 4 and the immediately following outbound pass on orbit 5, following recovery of PSD at high L*. However, this only accounts for around half an order of magnitude in additional loss, much smaller than the earlier losses which we attribute to outward ULF wave transport. Significantly, these two orbital segments are associated with significant and dynamic changes in the background magnetic field and span the period of the impact of a large

solar wind sudden impulse as described in Ref. 1. This can be seen not only in large $\sim \! 10\%$ fluctuations of the ratio of B_{loc} / B_{mea} , but also in large differences between the observed fields at the closely spaced Van Allen Probes A and B at this time - but which are not observed at other times.

The arrival of the impulse pushes the magnetopause inwards, and is expected to drive strong ULF waves. Such large amplitude field fluctuations can also drive non-diffusive and more coherent transport (Mann et al., 2013), which unlike diffusion does not rely on, nor necessarily generate, monotonic PSD profiles (e.g., Degeling et al., 2008; Ukhorskiy et al., 2006). Evidence for such non-monotonic, even double peaked, PSD distributions are seen in outbound orbit 6 at both μ (Figure 1, and Supplementary Figures 3, 4, 5 and 6). It is possible that the magnetospheric compression also drives intense EMIC waves, as described for example by Usanova et al. (2008; 2010), and these EMIC waves could also play a role in this subsequent smaller magnitude local loss. However, the dip appears to be more distinct at $K = 0.05 \text{ G}^{0.5}R_{\text{F}}$ than 0.1 $G^{0.5}R_{\text{F}}$, which is perhaps the opposite of what would be expected given that EMIC waves preferentially interact with higher pitch angle particles and cannot on their own drive losses to the core of the distributions at lower K (e.g., Usanova et al., 2014). Interestingly, as shown Supplementary Figures 3, 4, 5 and 6, the energy of the particles in the PSD dip at 2500 MeV/G and 3500 MeV/G at this time are around ~3 MeV and ~3.5 MeV, respectively, and these energy channels are close to the noise floor at that L* value and above at this time. Finally, this period is also associated with a similar model underestimate of the local field at higher L* described earlier, perhaps generating further errors in the inferred L*-dependence of the PSD profiles.

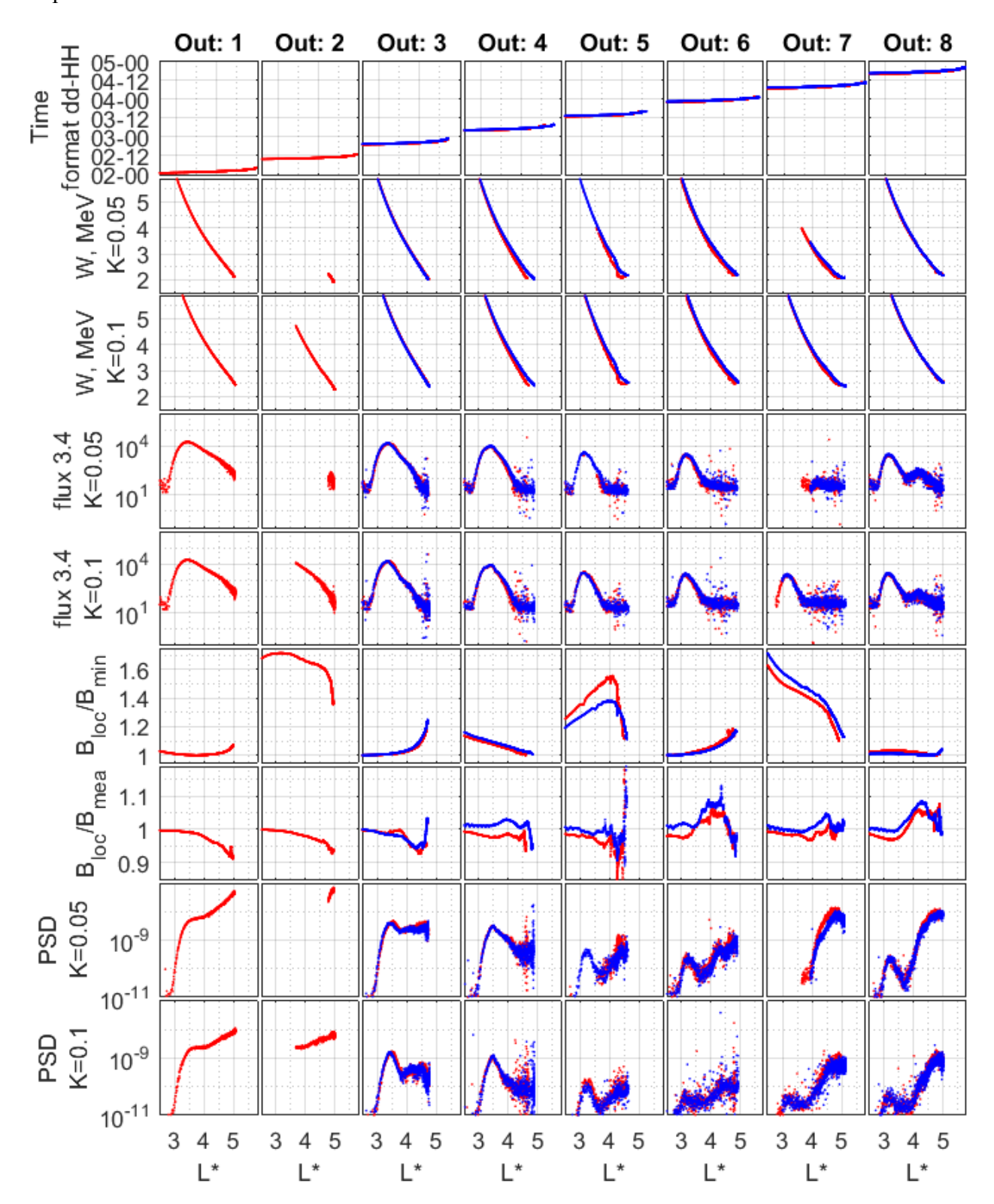
We emphasise that in deriving our PSD profiles at fixed first and second adiabatic invariants, we paid very close attention to both the limits of the lowest energies available from

the REPT instrument, and the limitations in K coverage due to off-equatorial elements of the Van Allen Probe orbits. We did interpolate the flux data in order to obtain PSD at fixed μ and K; however, we have not extrapolated beyond either the available energy range of the data from the REPT instrument, or beyond the lowest K measureable by the probes, at any time. Overall, and in our view, the PSD profiles we show here are consistent with the conclusion that the major losses which create the remnant belt arise from outwards transport, and not from the action of EMIC waves.

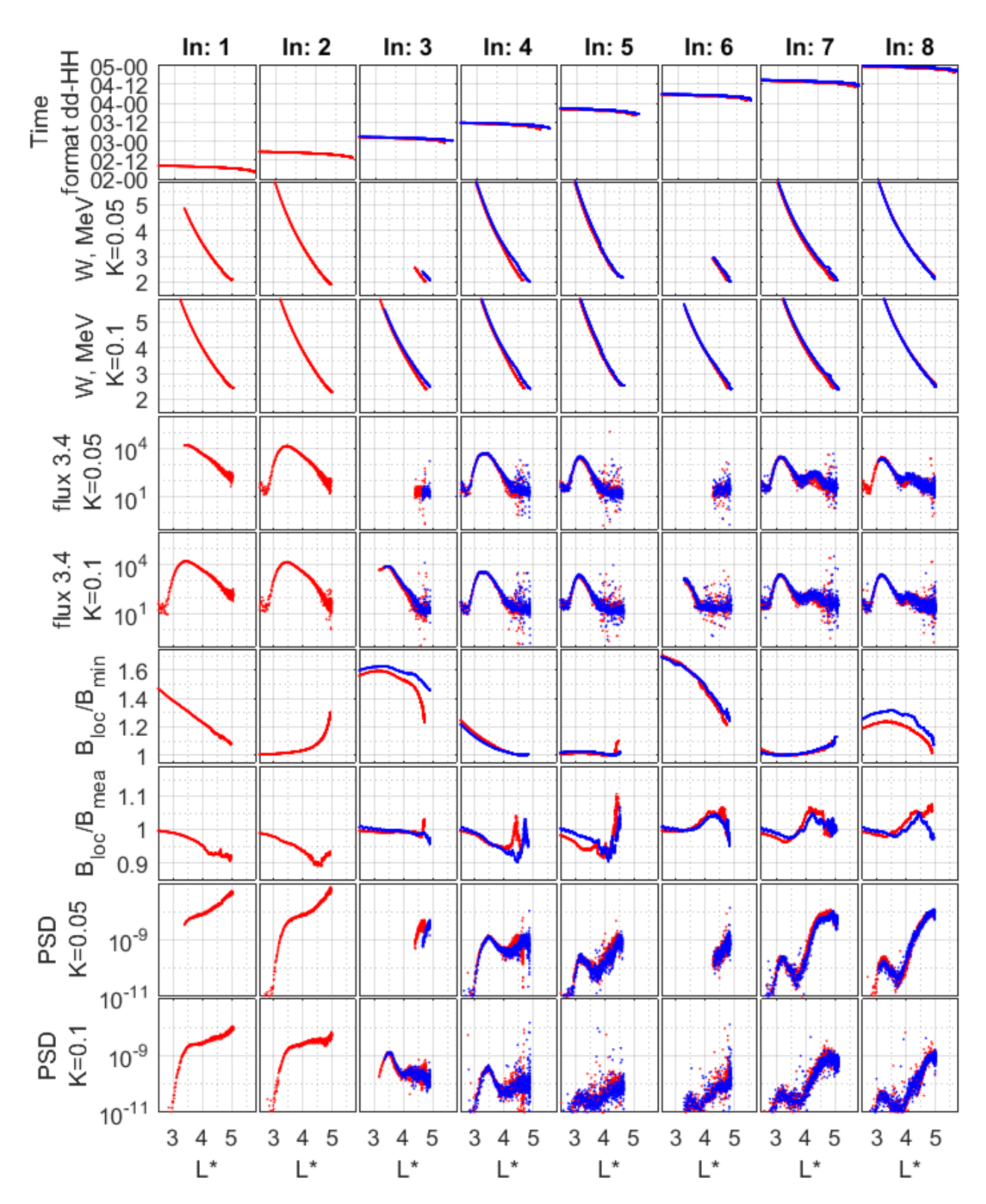
Energy Dependent Electron Flux Dynamics at the Outer Boundary

To examine the nature of the flux change and shadowing seen by other spacecraft at altitudes above the apogee of the Van Allen Probes, Supplementary Figure 7 shows observations from selected Los Alamos National Laboratory (LANL) geosynchronous spacecraft showing evidence for genuine flux loss associated with magnetopause shadowing. During the initial period of depletion, the LANL flux data shows a clear L* dependence with LANL 1994-084 and LANL-01A observing flux loss at high L* beginning around 4 UT on 2nd September, but with LANL-97A at lower L* only observing the loss around 8 hours later. The inward L* propagation of the loss points strongly to the importance of magnetopause shadowing. In direct contrast, and without presenting any observational support for the existence of EMIC waves in the correct L* range, this is the same period where S13 introduce EMIC waves. Specifically, S13 assert that there is a prolonged and continuous action of EMIC wave losses on L-shells as low as L=3 lasting for a total of 51 hours between "00 UT of September 3 and 03 UT of September 5" and which they claim creates the third belt. Similar observations from the GPS constellation, using the approach defined by Morley et al. (2016; 2017) using data from the Combined X-ray Dosimeter (CXD; Tuszewski et al., 2004) and presented in Supplementary Figures 8 and 9

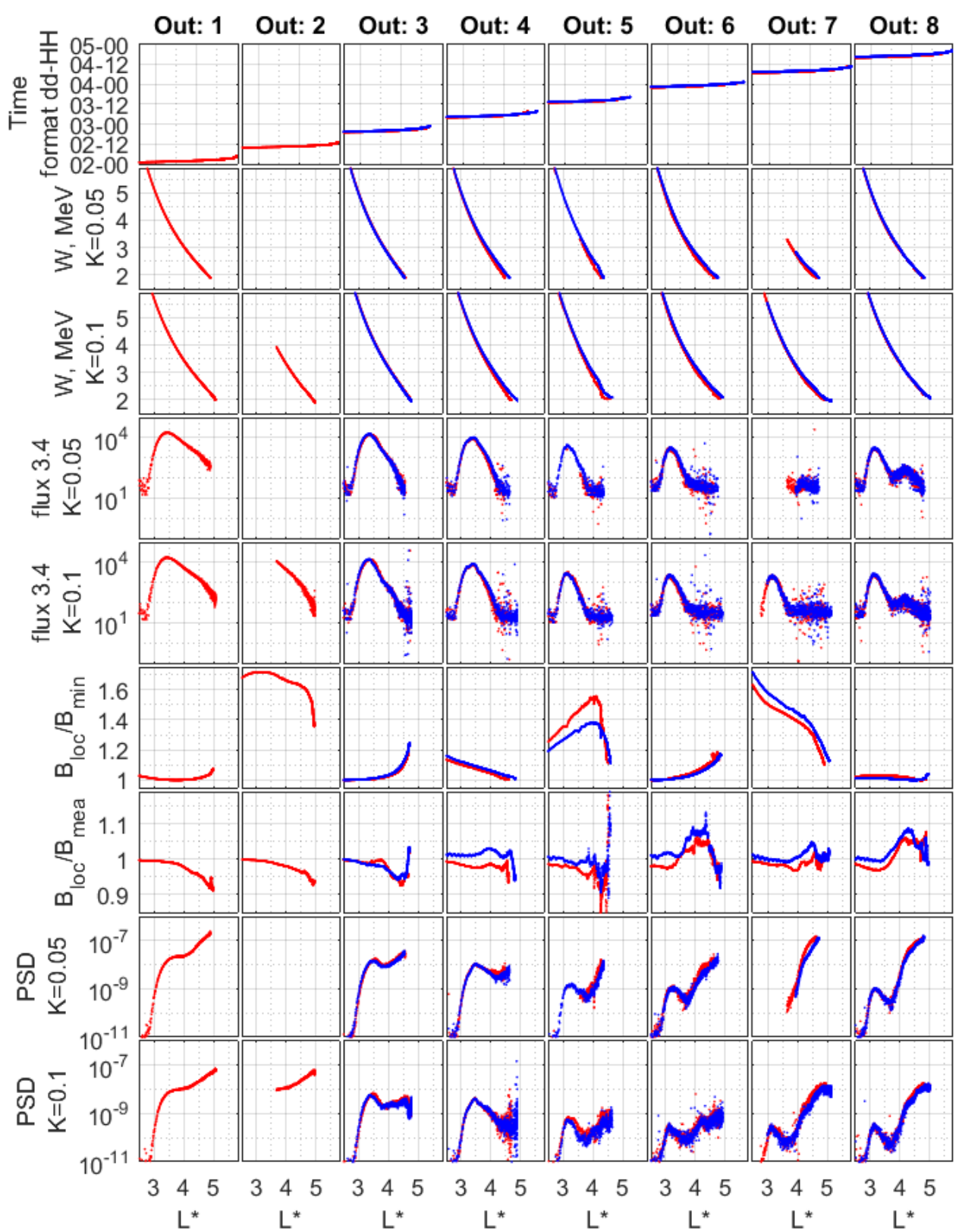
below, also show evidence consistent with magnetopause shadowing occurring over the period required to create the remnant belt.



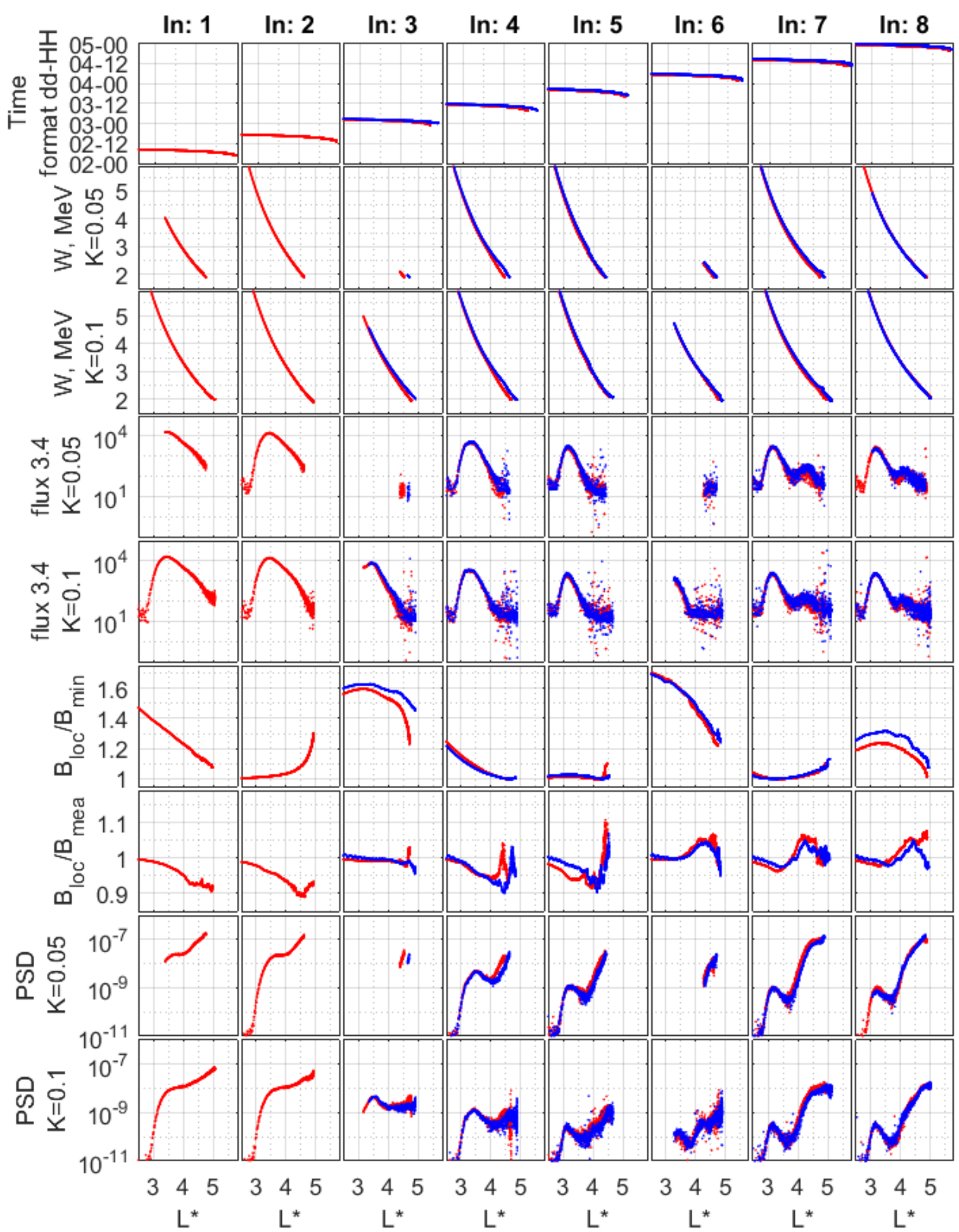
Supplementary Fig. 3. Equatorial PSD profiles at fixed $K = 0.05 \, G^{0.5} R_E$ and $0.1 \, G^{0.5} R_E$ (bottom two rows) at fixed μ =3500 MeV/G from outbound passes of Van Allen Probes A and B. Rows (in order) show: the time of each orbital pass; the energy of the particles at these K; the flux of 3.4 MeV energy particles at these K (/MeV/cm²/s/sr); the ratio of the TS04D model magnetic field at the spacecraft location (Bloc) and at the equator (Bmin); the ratio of Bloc to the magnetic field measured by the probes; and the PSD at fixed $K = 0.05 \, G^{0.5} R_E$ and $0.1 \, G^{0.5} R_E$ for μ = 3500 MeV/G. Van Allen Probes A and B are shown in red and blue, respectively. Supplementary Figure 2 shows the inbound passes at 3500 MeV/G, and Supplementary Figures 3 and 4 show the out- and in-bound passes at 2500 MeV/G in the same format. At times the offequatorial latitude of the satellite limits the range of measureable K; for example, during outbound orbit 2 the minimum K is above $0.05 \, G^{0.5} R_E$ for almost the whole pass. The losses associated with decreasing PSD profiles with L^* at outbound orbits 3 and 4 are consistent with outward radial transport. The underestimate of the model magnetic field compared to observations may further reduce the PSD at $L^* > \sim$ 4 on outbound orbit 3, further validating the outward transport hypothesis. See text for details.



Supplementary Fig. 4. Equatorial PSD profiles at fixed $K = 0.05 \, G^{0.5} R_E$ and 0.1 $G^{0.5} R_E$ (bottom two rows) at fixed μ =3500 MeV/G from inbound passes of Van Allen Probes A and B. Same format as Supplementary Figure 3.



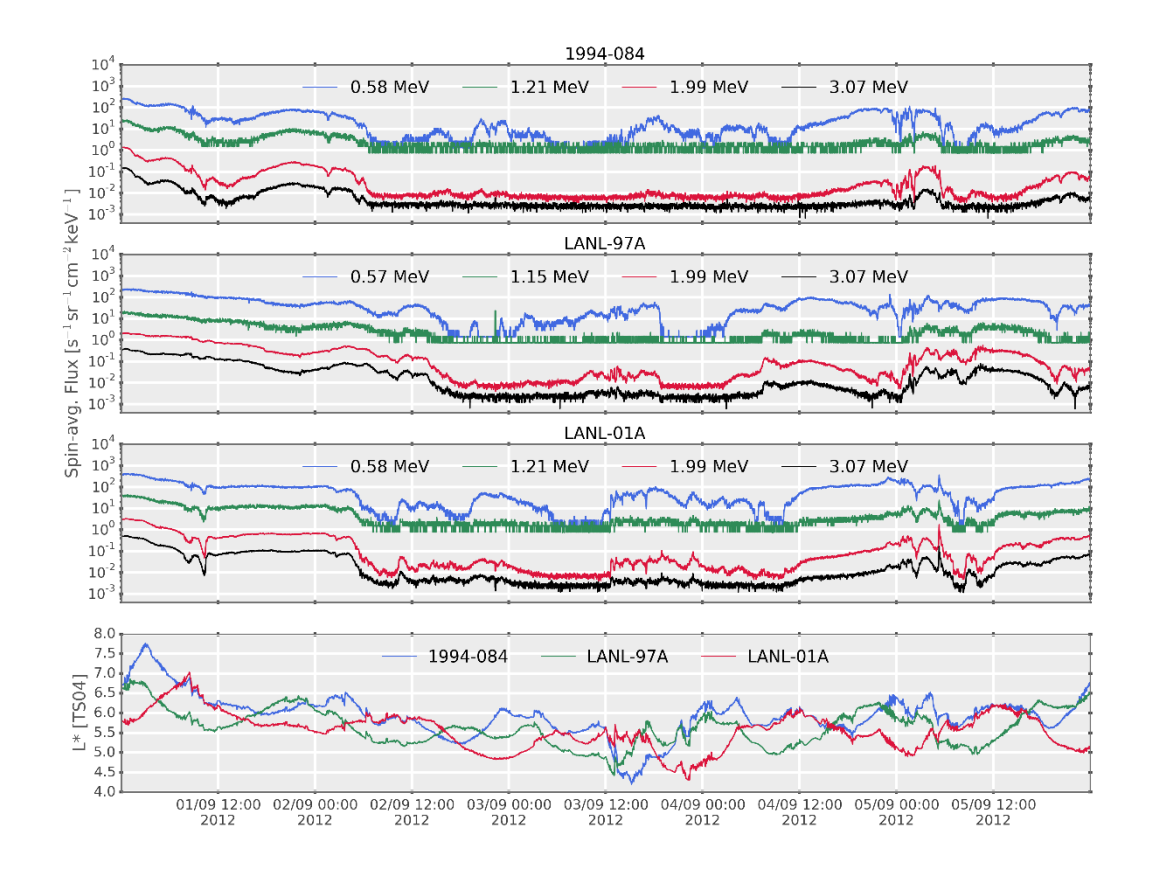
Supplementary Fig. 5. Equatorial PSD profiles at fixed $K = 0.05 \, G^{0.5} R_E$ and 0.1 $G^{0.5} R_E$ (bottom two rows) at fixed μ =2500 MeV/G from outbound passes of Van Allen Probes A and B. Same format as Supplementary Figure 3.



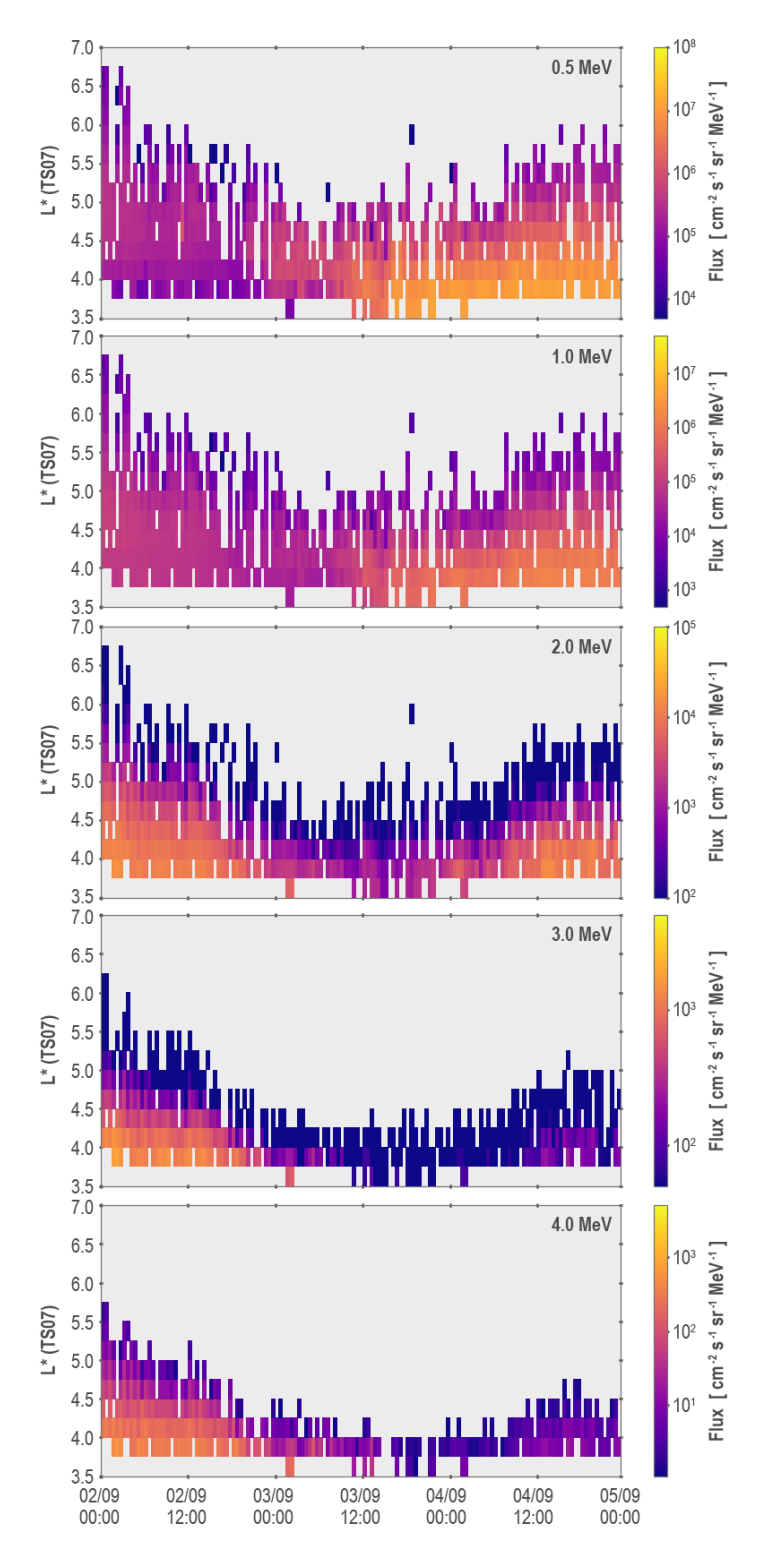
Supplementary Fig. 6. Equatorial PSD profiles at fixed $K = 0.05 G^{0.5}R_E$ and 0.1 $G^{0.5}R_E$ (bottom two rows) at fixed μ =2500 MeV/G from inbound passes of Van Allen Probes A and B. Same format as Figure 2 in the main article of our reply.

Supplementary Figure 7 shows the differential flux at five selected energies and which can be monitored at high temporal (~ 30 minutes) and high spatial (~ 0.25 Earth radii) resolution by combining data from the Combined X-ray Dosimeter (CXD; Tuszewski et al., 2004) detectors on the network of Global Positioning System (GPS) satellites as a function of L*. Here data from seven GPS satellites were combined, and L* was calculated from the Sitnov *et al.* (2008; hereafter TS07) magnetic field model (for comparison with the S17 Comment) assuming a locally mirroring population. Note that at L* of around 4 the detectors monitor the entire pitch angle distribution, but at higher L* particles mirroring below the spacecraft are missed such that CXD is measuring the distribution at somewhat lower pitch angles (see Morley *et al.* (2016; 2017) for more details).

The trends of relativistic and ultra-relativistic dynamics seen at higher L* by the LANL satellites shown in Supplementary Figure 7 above are verified across a range of L* in the flux observed by GPS in Supplementary Figure 8, further demonstrating that there is an outer boundary flux depletion consistent with magnetopause shadowing. In addition, and as with the LANL geosynchronous data, a clear inwards propagation of loss is seen in Supplementary Figure 8 and this is especially clear at the higher energies. However, and as seen by both LANL and GPS, at the outer boundary of the belt the lower energy fluxes are depleted less and recover more quickly than electrons at higher energies. Likely this is related to additional processes such convective transport and electron injections affecting lower energy electron populations, for example during substorm activations which are seen during this period. Nonetheless, both the GPS and LANL data provide evidence for the importance of outward ULF wave radial diffusion and magnetopause shadowing related losses at this time, consistent with the original conclusions in Mann et al., (2016).

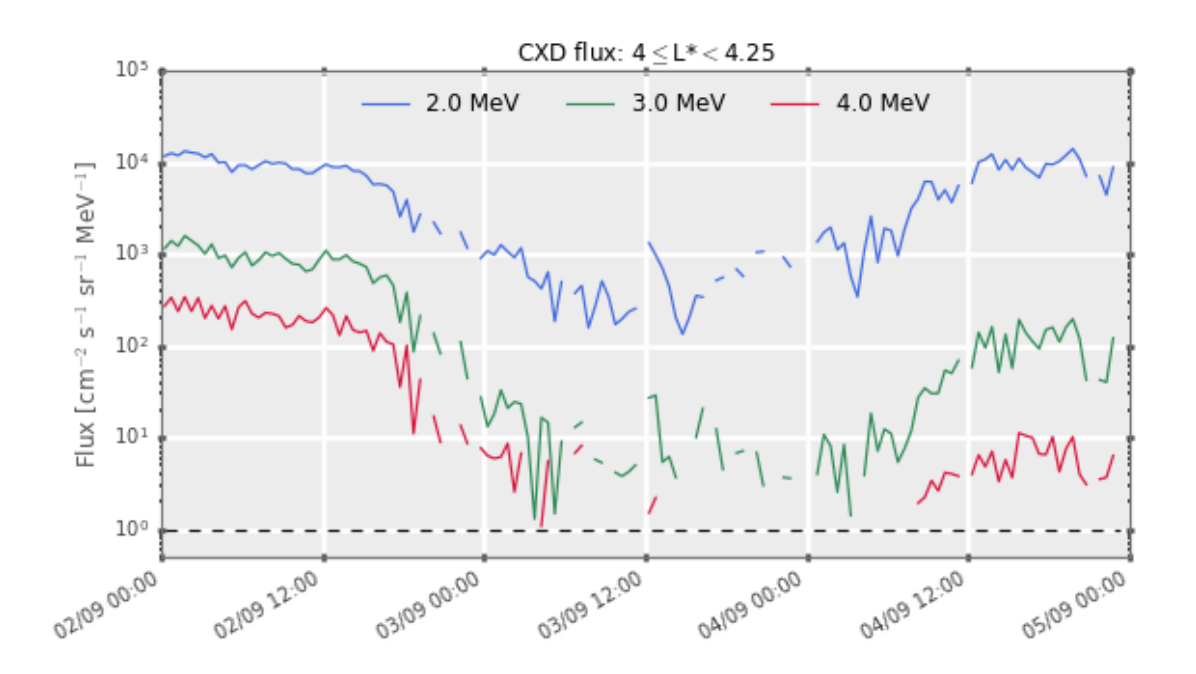


Supplementary Fig. 7. Los Alamos National Laboratory (LANL) geosynchronous satellite differential flux. Fluxes at energies of 0.58 MeV and 1.21 MeV (from the Synchronous Orbit Particle Analyzer (SOPA) instrument; Belian et al., 1992) and from 1.99 MeV and 3.07 MeV (from the Energy Spectrometer for Particles (ESP) instrument; e.g., Meier et al., 1996) from the 1994-084 (top panel; geographic longitude 49 degrees West), LANL-97A (second panel; geographic longitude 21 degrees East) and LANL-01A (third panel; geographic longitude 165 degrees West) satellites showing the drop-outs of electron flux by several orders of magnitude during the shadowing interval and which reach the instruments noise floor for extended periods. The lower energy (0.58 MeV) flux is depleted for a shorter period than at higher energies. L* as a function of time for each of the satellites in the first three panels (bottom panel) derived using the TS04 (Tsyganenko and Sitnov, 2004) magnetic field model computed with the neural network approach (Yu et al., 2012, and references therein).



Supplementary Fig. 8. Differential energy flux observed by the GPS constellation. Differential energy flux observed by the CXD instrument combined from 7 GPS satellites as a function of L* (TS07 magnetic field model) for five different energy channels (from top to bottom): 0.5 MeV, 1.0 Me, 2.0 MeV, 3.0 MeV, and 4.0 MeV. Inward propagation of loss as function of L* and time at high resolution is clearly seen in the combined data from the GPS constellation. The flux is also depleted for longer and more deeply at higher energies.

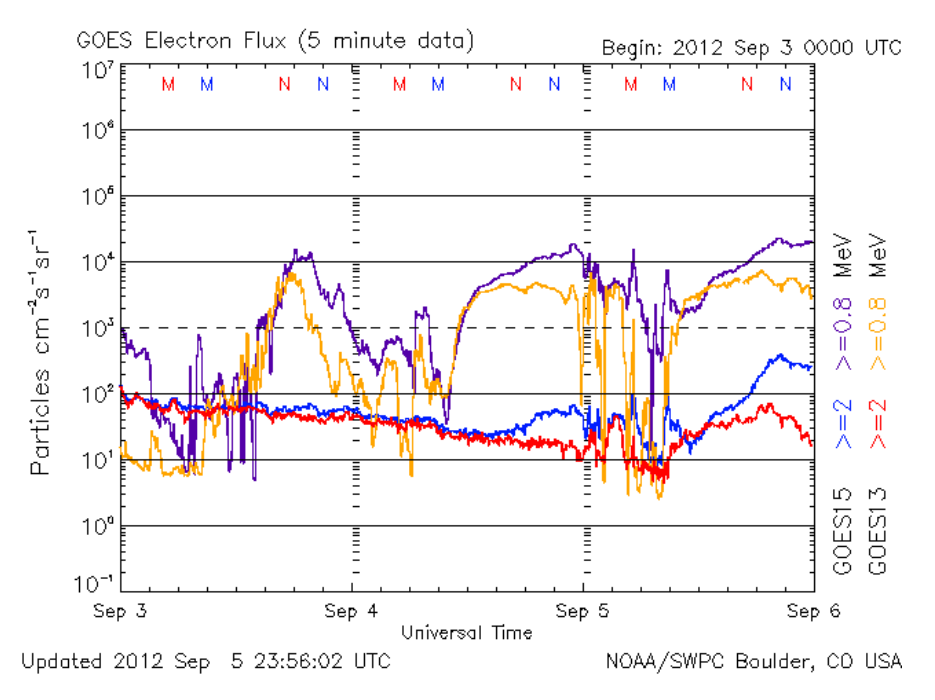
To illustrate this further, Supplementary Figure 9 shows time-series of data combined from the CXD instrument on-board seven satellites in the GPS constellation at ultra-relativistic energies between 2.0-4.0 MeV during the third-belt interval. The CXD data shows clearly the depletion of flux at these energies in the L* bin from $L^* = 4.0 - 4.25$ at the same time as the depletion shown in Supplementary Figure 8. This further demonstrates that magnetopause shadowing and outwards ULF wave radial diffusion can explain the losses needed to create the third radiation belt.



Supplementary Fig. 9. Ultra-relativistic flux from the GPS constellation. Time series of GPS CXD data derived from seven spacecraft at three ultra-relativistic energies (2.0 MeV (blue), 3.0 MeV (green), and 4.0 MeV (red)) from 00 UT on September 2^{nd} to 00 UT on September 5^{th} binned in the L* range $4.0 < L^* < 4.25$ (TS07 model) (the instrument noise floor is estimated at $1 \text{ cm}^2 \text{s}^{-1} \text{sr}^{-1} \text{ MeV}^{-1}$ and is shown as the black dashed line).

Coupling Between the Outer Boundary Condition and Low L* Radiation Belt Dynamics

As discussed recently by Mann and Ozeke (2016), an accurate specification of the outer boundary condition is absolutely essential to accurately assess the impacts of ULF wave radial transport. Indeed, as shown by Mann and Ozeke (2016) under conditions of strong ULF wave power during magnetopause shadowing intervals the losses from outwards ULF wave transport can penetrate much more deeply and much more quickly into the heart of the radiation belts (on timescales of ~ hours) than previously thought. As shown in Supplementary Figure 1, such ULF transport can cause outwards radial diffusion losses which create the remnant belt in less than 1 day. If the dynamics of the flux at the outer boundary are a strong function of energy, then it is also possible for the same ULF waves to create both acceleration (through inward transport) and loss (through outward transport) at different energies/first adiabatic invariants at the same time.



Supplementary Fig. 10. Integral electron flux from GOES geosynchronous satellites. Integral electron flux in the > 800 keV and > 2 MeV energy channels from GOES 15(purple and blue, respectively) and GOES 13 (gold and red, respectively) for three days from 00 UT on September 3^{rd} to 00 UT on September 6^{th} . There is a clear difference between the long-lasting depletion of the > 2 MeV electron flux and the faster recovery of the lower energy > 800 keV integral electron flux especially following 12 noon on September 3^{rd} . Local Noon (N) and local midnight (M) are shown for each satellite.

S17 cite S13 in support of their conclusions, with the S13 modelling showing that when EMIC waves are introduced at low L, down to L=3, this can create a third belt

morphology. However, in the S13 modelling the effects from magnetopause shadowing are likely to be significantly underestimated. The modelling work presented by S13 states (their Supplementary Material, page 3) that in their model "the [outer] boundary condition is set up from GOES data". How GOES data is used to constrain the flux at a fixed outer boundary location at fixed L*=6.3 in the S13 modelling, at an L* location much higher than GOES, is not explained. At relativistic energies the only GOES data which is available to specify the flux at the outer boundary in S13 is in two integral energy channels at > 800 keV and > 2 MeV (there is an integral energy channel at > 4 MeV but this channel appears to be at the noise floor). Supplementary Figure 10 shows these integrated electron flux channels from the geosynchronous GOES13 and GOES15 satellites, and as shown in the original Mann et al. (2016) article, the GOES > 2 MeV integral flux is reduced to the effective noise floor until around the middle of 5th September. During magnetopause shadowing intervals the flux at lower L* will also likely be much larger than that at higher L* such that using GOES flux to constrain the dynamics at a fixed L*=6.3 as is done in S13 will likely very significantly underestimate the impact arising from magnetopause shadowing and outward radial diffusion. Given the energy dependence of the flux at the outer boundary, and the likely underestimate of the losses arising from outward ULF transport and magnetopause shadowing, it is perhaps not surprising that S13 required the addition of some extra losses through a representation of effects arising from EMIC waves in order to create a third belt in their model.

References

Baker, D. N. et al. A long-lived relativistic electron storage ring embedded in Earth's outer Van Allen belt. *Science* 340, 186-190 (2013).

Belian, R. D., et al., High-Z energetic particles at geosynchronous orbit during the great solar proton event series of October 1989, *J. Geophys. Res.*, 97, 16,897–16,906 (1992).

Brautigam, D. & Albert, J. Radial diffusion analysis of outer radiation belt electrons during the October 9, 1990, magnetic storm. *J. Geophys. Res.* 105, 291-309 (2000).

Degeling, A. W., et al. Drift resonant generation of peaked relativistic electron distributions by Pc 5 ULF waves. *J. Geophys. Res.*, 113.A2 (2008).

Dimitrakoudis, S., et al. Accurately specifying storm-time ULF wave radial diffusion in the radiation belts. *Geophys. Res. Lett.* 42, 5711-5718 (2015).

Mann, I. R. et al., Explaining the dynamics of the ultra-relativistic third Van Allen radiation belt, *Nature Physics*, (2016).

Mann, Ian R., et al. Discovery of the action of a geophysical synchrotron in the Earth's Van Allen radiation belts. *Nature Communications*, 4, 2795 (2013).

Mann, I. R., and L. G. Ozeke. How quickly, how deeply, and how strongly can dynamical outer boundary conditions impact Van Allen radiation belt morphology? *J. Geophys. Res.* (2016).

Mauk, B. H., et al. Science objectives and rationale for the radiation belt storm probes mission. *Space Sci. Rev.* 179, 3-27 (2013).

Meier, M.-M., et al. The energy spectrometer for particles (ESP): Instrument description and orbital performance. AIP Conference proceedings. (1996).

Morley, S. K., et al. The Global Positioning System constellation as a space weather monitor: Comparison of electron measurements with Van Allen Probes data. Space Weather, 14(2), 76-92 (2016).

Morley, S. K., et al., Energetic particle data from the Global Positioning System constellation, Space Weather, 15, 283–289, doi:10.1002/2017SW001604 (2017).

Murphy, K. R., et al. Accurately characterizing the importance of wave-particle interactions in radiation belt dynamics: The pitfalls of statistical wave representations. J. Geophys. Res. 121, 7895-7899 (2016)

O'Brien, T. P., et al. On the use of drift echoes to characterize on-orbit sensor discrepanc ies. *J. Geophys. Res.*, 120.3, 2076-2087 (2015).

Shprits, Y. Y. et al. Comment on Mann et al, (2016). *Nature Physics*, this issue, (2017).

Shprits, Y. Y. et al. Unusual stable trapping of the ultra-relativistic electrons in the Van Allen radiation belts. *Nature Physics* 9, 699–703 (2013).

Sitnov, M. I., N. A. Tsyganenko, A. Y. Ukhorskiy, and P. C. Brandt. Dynamical data-based modeling of the storm-time geomagnetic field with enhanced spatial resolution, J. Geophys. Res., 113, A07218, doi:10.1029/2007JA013003 (2008).

Tsyganenko, N. A. and M. I. Sitnov. Modeling the dynamics of the inner magnetosphere during strong geomagnetic storms, *J. Geophys. Res.*, 110, A03208, doi:10.1029/2004JA010798 (2005).

Tuszewski, M., et al., Bremsstrahlung effects in energetic particle detectors, Space Weather, 2, S10S01, doi:10.1029/2003SW000057 (2004).

Ukhorskiy, A. Y., et al. Storm time evolution of the outer radiation belt: Transport and losses. *J. Geophys. Res.*, 111.A11 (2006).

Usanova, M. E., et al. Multipoint observations of magnetospheric compression-related EMIC Pc1 waves by THEMIS and CARISMA. *Geophys. Res. Lett.*, 35.17 (2008).

Usanova, M. E., et al. Conjugate ground and multisatellite observations of compression-related EMIC Pc1 waves and associated proton precipitation *J. Geophys. Res.*, 115.A7 (2010).

Usanova, M. E., et al. Effect of EMIC waves on relativistic and ultrarelativistic electron populations: Ground-based and Van Allen Probes observations. *Geophys. Res. Lett.*, 41.5, 1375-1381 (2014).

Yu, Y., et al. L* neural networks from different magnetic field models and their applicability. *Space Weather* 10.2 (2012).